Lithospheric structure of an incipient rift basin: Results from receiver function analysis of Bransfield Strait, NW Antarctic Peninsula

C. Berk Biryol[a,*], Stephen J. Lee[b], Jonathan M. Lees[a], Michael J. Shore[a]

[a] Department of Geological Sciences, University of North Carolina at Chapel Hill, NC 27599, USA
[b] U.S. Army Research Laboratory/Army Research Office, Research Triangle Park, NC 27709, USA

ARTICLE INFO

Keywords:
Receiver function
Lithosphere
Moho
Slab window
Rift basin

ABSTRACT

Bransfield Basin (BB), located northwest of the Antarctic Peninsula (AP) and southeast of the South Shetland Islands (SSI), is the most active section of the Antarctic continental margin. The region has long been (50 Ma) a convergent plate boundary where the Phoenix plate was subducting beneath the Antarctic Plate and is characterized by long-lived arc magmatism and accretion. However, the collision of the Antarctic-Phoenix spreading center with the subduction front near SSI (ca. 4 Ma) gave way to the opening of slab windows and dramatic decrease in the subduction rate of the Phoenix plate beneath AP and SSI. Consequently, the Phoenix slab began to rollback slowly along the South Shetland Trench (SST), giving way to slow extension in the back-arc region and rifting along the BB. Although there is consensus on the factors that control the current deformation and extension of the BB, the origin of the BB and the tectonic configuration of the basin are still unclear. Most of the controversy stems from uncertainties regarding the crustal thickness of the BB. Hence, we computed teleseismic receiver functions for 10 broadband stations in the region that belong to existing permanent and temporary deployments in order obtain robust constraints on the lithospheric structure and crustal thickness of the BB, as well as the AP and SSI. Our results indicate that the crust is thinning from 30 km to 26 km from the AP towards the South Shetland trench and Central BB showing the asymmetrical character of the rift basin. The crustal thickness and Vp/Vs variations are less pronounced along the AP but very significant across the SSB indicating the lithospheric scale segmentation of the South Shetland Block (SSB) and the incipient rift basin under the control of the opening of slab window and the roll-back of stalled Phoenix slab. High Vp/Vs ratios (~1.9) beneath BB and SSI, agree well with the nascent rift character of BB, the presence of a steep Phoenix slab and consequently a wider mantle wedge characterized by the presence of underplating partial melts beneath SSI and BB.

1. Introduction

Subduction plate margins are sites of key Earth processes that include an abundance of destructive Earthquakes, recycling of oceanic lithosphere, arc volcanism and volcanic eruptions, as well as continental growth. Hence, they contribute significantly to our understanding of the Earth's structure and processes. However, various complications can alter the usual pattern of these processes and how they operate. One of these complications is the existence of windows in the lithosphere (slab) descending into the mantle due to subduction of spreading ridges (Thorkelson, 1996). The initiation and widening of such a gap in the slab may lead to a major reconfiguration of the plate margin, significant changes in the character of tectonism. Today, various subduction segments along the Pacific margin of the North and South America Plates display these effects clearly where spreading centers subduct beneath these plates (i.e. Western U.S., Mexico, Costa Rica, Patagonia) (McCrory et al., 2009). However, the relationships between attributes of the slab windows and the deformation and reconfiguration of the plate margin remain unclear (van Wijk et al., 2001; Guillaume et al., 2010). The opening of gaps in the slab in a convergent plate margin can also lead to the gradual demise of the convergence and subduction in the remnant part of the convergent plate margin. A good example for slab window opening and stalled subduction is located at the northwestern margin of Antarctica Plate. Various studies have linked the significant tectonic reconfiguration of the Antarctica Plate margin and cessation of subduction in the vicinity of the Bransfield Strait to the opening of a slab window beneath the Antarctic Peninsula (Hole and Larter, 1993; Barker and Austin, 1998). Hence, this is a premier location to study characteristics of slab windows and stalled subduction as well as their contribution to factors that govern the

---

[*] Corresponding author.
E-mail address: biryol@live.unc.edu (C.B. Biryol).

https://doi.org/10.1016/j.polar.2018.02.003
Received 25 October 2017; Received in revised form 26 January 2018; Accepted 16 February 2018

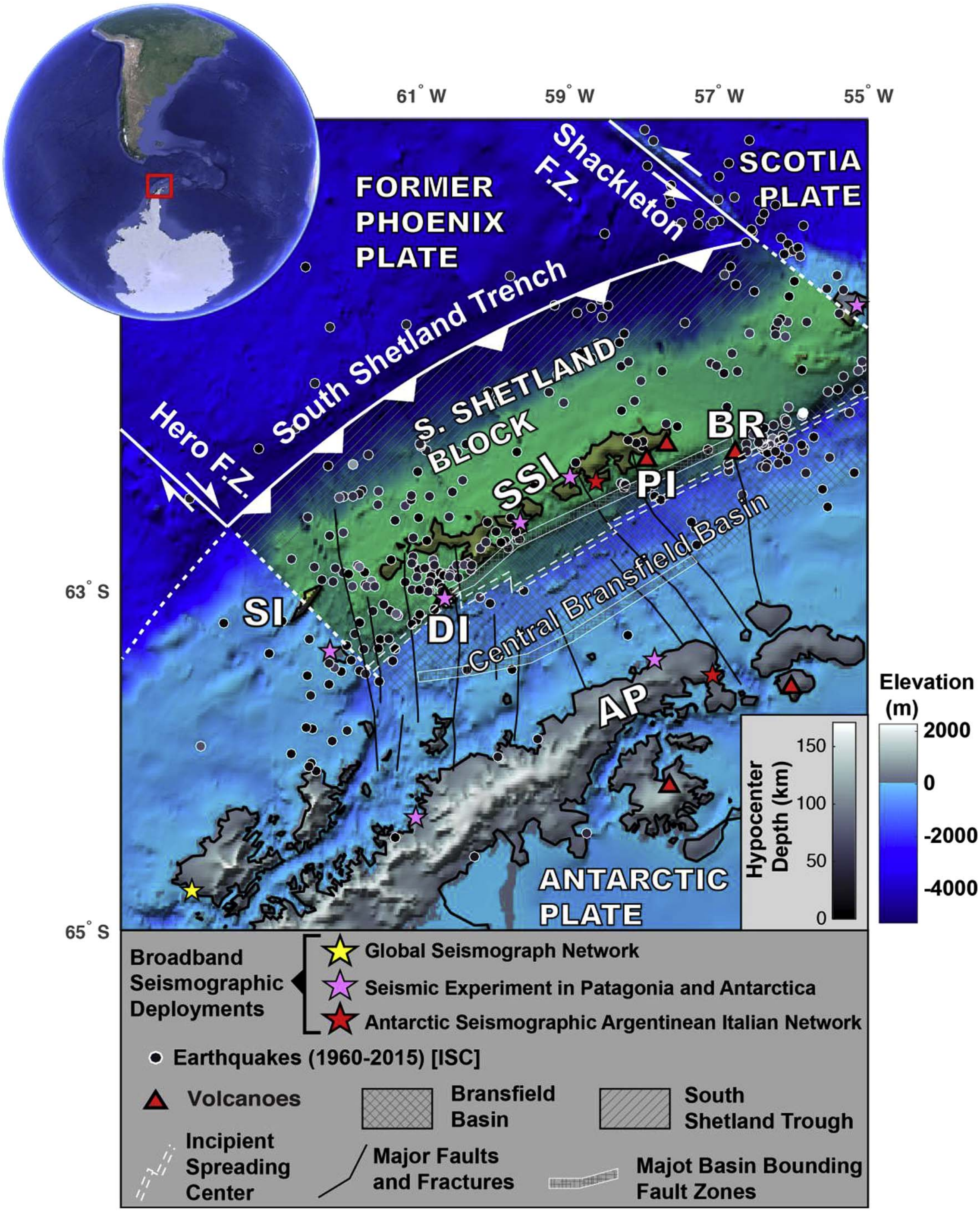

Fig. 1. Map of the Bransfield Strait, the South Shetland Islands, and the Antarctic Peninsula. The map shows locations and affiliations of seismic deployments in the region as well as the locations of major volcanic centers and earthquakes retrieved from the International Seismological Center (ISC) catalog. Major fractures, faults, and basin bounding fault zones are also illustrated (Grad et al., 1992). Plate boundaries and major tectonic features are illustrated by white lines. The SSB is shaded in green. DI = Deception island; PI = Penguin Island; BR = Bridgeman Island; SI = Smith Island.

rheology, volcanism, and tectonism of the associated plate margin and the Bransfield Straight.

The Bransfield Straight hosts the Bransfield Basin (BB), and the region is one of the most active sections of the Antarctica Plate (Maurice et al., 2003). The Antarctic Peninsula (AP) to the southeast and South Shetland Islands (SSI) to the northwest border the basin (Fig. 1). The current geology and the structure of the region are partly governed by the long-lived plate convergence and subduction of the Phoenix Plate southeastward beneath the Antarctica Plate (Dalziel, 1984; Keller et al., 1991). This region is thus characterized by prolonged arc magmatism and accretion, giving way to metamorphism and uplift of Mesozoic-Cenozoic accretionary wedge material that forms the AP and SSI (Birkenmajer et al., 1986; Machado et al., 2005). Upon collision of the Antarctic-Phoenix spreading center with the subduction front near SSI (ca. 4 Ma), spreading deactivated and the oceanic Phoenix plate became a part of the Antarctic Plate (Barker and Dalziel, 1983; Larter and Barker, 1991). The collision of the spreading center gave way to the opening of slab windows where the subduction trench meets the spreading ridge (Hole and Larter, 1993). After the cessation of spreading along the Phoenix-Antarctic spreading ridge, subduction of the Phoenix plate beneath AP and SSI slowed down dramatically and the Phoenix slab began to rollback slowly along the South Shetland Trench (SST) towards the Pacific. As a consequence of inter-plate coupling, the rollback of the Phoenix slab gave way to slow extension in the back-arc region and opening (rifting) of the BB (Gonzalez-Ferran, 1985; Galindo-Zaldivar et al., 2004).

Various attributes of the overriding plate such as the thickness of the crust, rheology and partial melt content provide important clues on how complexities in the subducting plate may be controlling the deformation of the plate margin in the vicinity of the subduction zone. The study of converted seismic phases (i.e. receiver functions) that sample major lithospheric structural boundaries yield valuable constraints on structural properties and compositional attributes of the lithosphere. Acquired receiver functions provide first peek at major lithospheric discontinuities such as the Moho and hence crustal thickness. These help in constraining the structural and compositional variations across lithospheric boundaries (i.e. volatile content, rheology).

We study the attributes of the lithosphere and asthenosphere beneath the Bransfield Strait via teleseismic P-wave Receiver Functions (RF). Our results provide valuable constraints on the structure; composition and partial melt content of the lithosphere of the region. Our results also reveal the present day structural configuration of the slab window and the slab following the stalled subduction. Furthermore, our results provide physical and compositional attributes of asthenosphere and lithosphere in this region, which is essential in the geodynamical modeling of the lithospheric deformation and isostasy in the region due to glacial dynamics.

1.1. *Tectonic setting*

The Bransfield Basin (BB) is a backarc basin and the major tectonic components of the region that control this basin are the Shetland Islands (island arc), South Shetland Trench (SST) and South Shetland Subduction Zone (SSSZ) (Keller et al., 1991). There are various active and extinct volcanic centers spread across the region that were mostly emplaced during Cenozoic-Mesozoic arc volcanism associated with the southeastward subduction of Phoenix plate (Smellie et al., 1984). Some of these volcanic centers are aligned, rather discontinuously, along and parallel to the axis of the Bransfield basin and display systematic variations in style of magmatism as well as compositions through the extent of the basin (Hole and Larter, 1993; Lawver et al., 1996; Gracia et al., 1996). Seamount volcanoes, neovolcanic ridges, cinder cones, and calderas constitute these volcanic centers. These volcanic centers have ages ranging between 0.3 and 2 Ma and are located at deeper parts of the submarine basin which is 2000m deep (Gracia et al., 1996; Lawver et al., 1996). The compositions of the volcanic rocks display a complex pattern of magmatism across the basin (Hole and Larter, 1993).

The BB displays an asymmetrical geometry with a steep northwestern limit controlled by high-angle normal faults (Galindo-Zaldivar et al., 2004) and a more gently sloping southeastern boundary. It is subdivided into three sub-basins, which are eastern, central and western sub-basins. The subdivisions are generally marked by changes in bathymetry and width. The Eastern BB (EBB) defines the narrowest segment of the basin while Western BB (NBB) is the widest segment. Based on geodetic data, the extension rate in the basin varies between 5 and 20 mm/yr and the extension has a NW-SE direction (Dietrich et al., 2001). Results from various studies indicate that the opening rate of the basin increased in the past 2 Ma (Gonzalez-Ferran, 1985) compared to Oligocene-Miocene rates that are in the order of 1.1 mm/yr (Sell et al., 2004). Important Pleistocene-Recent fractures are associated with prominent volcanic centers of the region, which are, from south to north, Deception Penguin and Bridgeman Islands/ridges (Gonzalez-Ferran, 1985) (see Fig. 1 for locations). The Central BB (CBB) has an intermediate width compared to the other segments but occupies the largest area and differentiates from the other sections with distinguishable seismicity, large coverage of seamount volcanism as well as deeper bathymetry (Gracia et al., 1996; Lawver et al., 1996). The CBB is roughly bounded by the extent of the South Shetland Block (SSB) or South Shetland Microplate. The extent of the SSB, on the other hand, is defined by the structural control imposed on the block by Hero and Shackleton Fracture zones that also control the bounds of SST, SSSZ and the former Phoenix Plate (Alfaro et al., 2010) (Fig. 1).

1.2. *South Shetland Block & incipient rifting*

The SSB is located in the volcanic arc region of the SSSZ (Birkenmajer et al., 1986; Machado et al., 2005; Majdański et al., 2008). The evolution of this block is directly related to the opening of the Bransfield Basin and the events that lead to it (Maurice et al., 2003; Majdański et al., 2008). One event that has an important contribution is the collision of Antarctic-Phoenix spreading center with the subduction front, located at the southwestward continuation of the SST. This event continued from 50 Ma to 4 Ma until spreading deactivated and the Phoenix plate became a part of the Antarctic Plate (Grad et al., 1992) (Fig. 1). The collision of the spreading center gave way to the opening of slab windows where the subduction trench meets the spreading ridge with unique compositions and patterns of volcanism (Hole and Larter, 1993; Breitsprecher and Thorkelson, 2009). After the cessation of spreading along the Phoenix- Antarctic spreading ridge, the subduction of Phoenix plate beneath AP and SSI slowed down dramatically and the Phoenix slab began to roll-back slowly along South Shetland Trench (SST) towards the Pacific.

The coupling of the plates requires that the overlying plate compensates the roll-back action which gave way to slow extension in the back-arc region and the opening of the BB (Lawver et al., 1995, 1996; Gracia et al., 1996). Although there is consensus on the origin of the BB, the current configuration of the basin is still unclear. Some studies suggest this basin initiated as an incipient rift basin, which is still in development (Lawver et al., 1995, 1996; Barker and Austin, 1998; Civile et al., 2012). Based on the presence of aligned but discontinuous seamount volcanism at the center of the basin some suggested that after a phase of incipient rifting the basin is now in the stage of incipient seafloor spreading (Ashcroft, 1972; Gracia et al., 1996). Most of this controversy sources from the lack of knowledge about the crustal thickness of the BB. Various active and passive source studies revealed significantly different thicknesses for the crust of the BB. These range from 7 to 30 km and points to the very complex character of the crust of the BB (Barker and Austin, 1998; Vuan et al., 2001; Baranov and Morelli, 2013; Hansen et al., 2014). Various studies revealed slower upper mantle beneath the crust but most of these studies suffered from limitations in resolution related to poor instrument coverage in the region (Vuan et al., 2001; Park et al., 2012).

2. Data and method

2.1. *Teleseismic P-waves*

The AP and the SSI hosts various broadband seismometer networks (Figs. 1 and 2c). However, the distribution of the associated stations is limited by the sparse presence of suitable land regions that are free of ice. We used available data from 10 stations located along the SSI and the northwestern edge of the AP (see Fig. 2c for the names and locations of these stations). 6 of these stations are located along the island arc (SSI, DI, Low Island and Elephant Island) and the remaining 4 are located along the AP. Although the distribution of the stations along the island arc is not uniform, they provide complete coverage of the northern margin of the BB for Northeast to Southwest margin. The 10 stations mainly belong to 3 different networks that operated in the region at different but overlapping periods of time (see Fig. 1 for names of networks). In case of temporary deployments, the operation periods

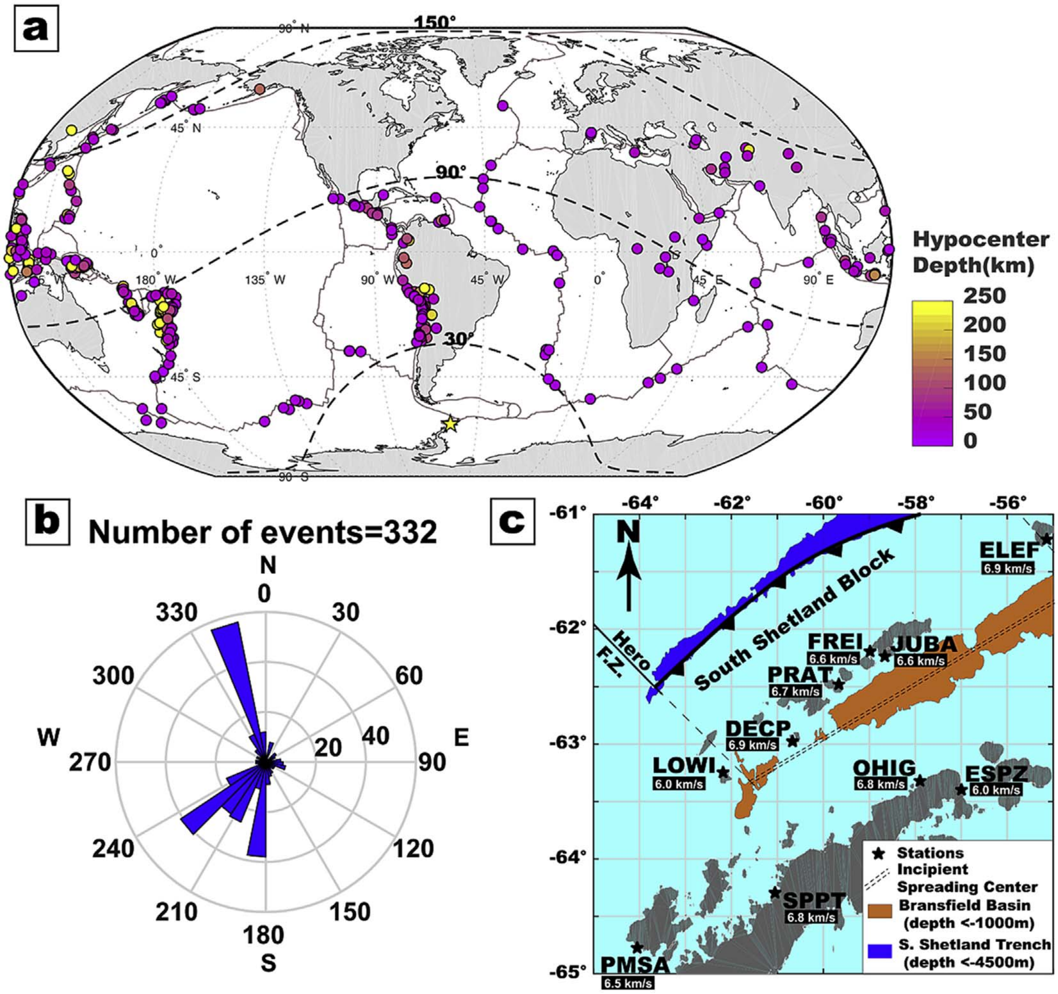

Fig. 2. Event and station locations for the dataset utilized in this study. **a.** Map of teleseismic earthquakes used in this study. We used P (distance = 30°–90°), PP (distance = 90°–150°) and PKP (distance = 120°–160°) and PKIKP (distance = 150°–180°) phases from these earthquakes. **b.** Rose diagram of back azimuths for the events shown in a. The dataset is dominated by the arrivals from subduction zone earthquakes to the NNW and SW. **c.** Map of stations and station names used for computing RF. The map also shows major tectonic features (i.e. incipient spreading center, Hero fracture zone) and the outlines of BB, Shout Shetland Trench and SSB for reference.

of these stations were limited by the Austral summer months (i.e. Seismic Experiment in Patagonia and Antarctica Deployment). Even though this significantly reduces the recording time of the stations, enough high-quality waveforms are available for us to proceed with calculation of the teleseismic P-wave receiver functions.

The data for our analysis is mainly seismograms of direct P waves from earthquakes located at a distance range from 30 to 90° away from each station (Fig. 2a). In order to maximize the number of calculated Receiver Functions (RF), to obtain the best possible sampling of the subsurface and to overcome the disadvantage of the limited operation time of some of the stations, we also incorporated PP and PKP and PKIKP phases in our analysis (Fig. 2a). Majority of the analyzed waveforms belong to earthquakes located at subduction zones to the NNW, S, and SW of the study area (Fig. 2b). The corresponding three component seismograms are windowed 5s before and 50s after the P wave arrival. The data is also band-pass filtered between 5 and 50s to maximize the signal content. Finally, the pre-processed data is quality controlled in order to obtain a reliable dataset with a relatively higher signal-to-noise ratio (Fig. 3).

2.2. *Receiver function analysis*

Receiver Functions (RFs) are time series, computed using the earthquake signals, which are recorded at three components of the seismometer (Radial, Transverse and Vertical components). Radial RFs are calculated using the radial- and vertical-component seismograms. These RFs show the relative response of the Earth structure at the receiver side (beneath the station). The deconvolution of the vertical component of the seismogram from the radial component provides elimination of the response of earthquake source and the instrument leaving behind the radial response of earth near the receiver. The resultant function contains composite series of P-to-S converted phases recorded at the station without any other redundant signal that does not belong to the receiver side (Ligorria and Ammon, 1999). The timing of the converted-phases primarily depends on the depth of the converting interface and the velocity structure between this interface and station (surface). The timing of different phases also depends on the path that they take in the crust. In order to be able to make the best use of information contained in RFs we use direct P-to-S converted phases (Ps) as well as the reverberation of this phase within the crust (PpPs and PsPs). The amplitudes of the converted phases depend on the incidence angle of the impinging wave as well as the velocity contrast across the interface where these are converted.

We used the iterative deconvolution algorithm of Ligorria and Ammon (1999) in order to obtain teleseismic RFs. This approach uses deconvolution of a series of Gaussian pulses from the input signals in the time domain and the width of each pulse controls the frequency content of the resulting receiver function. We calculated receiver functions using a Gaussian pulse width corresponding to low pass filter with a corner frequency of 2.5 Hz (Fig. 3). Furthermore, in order to

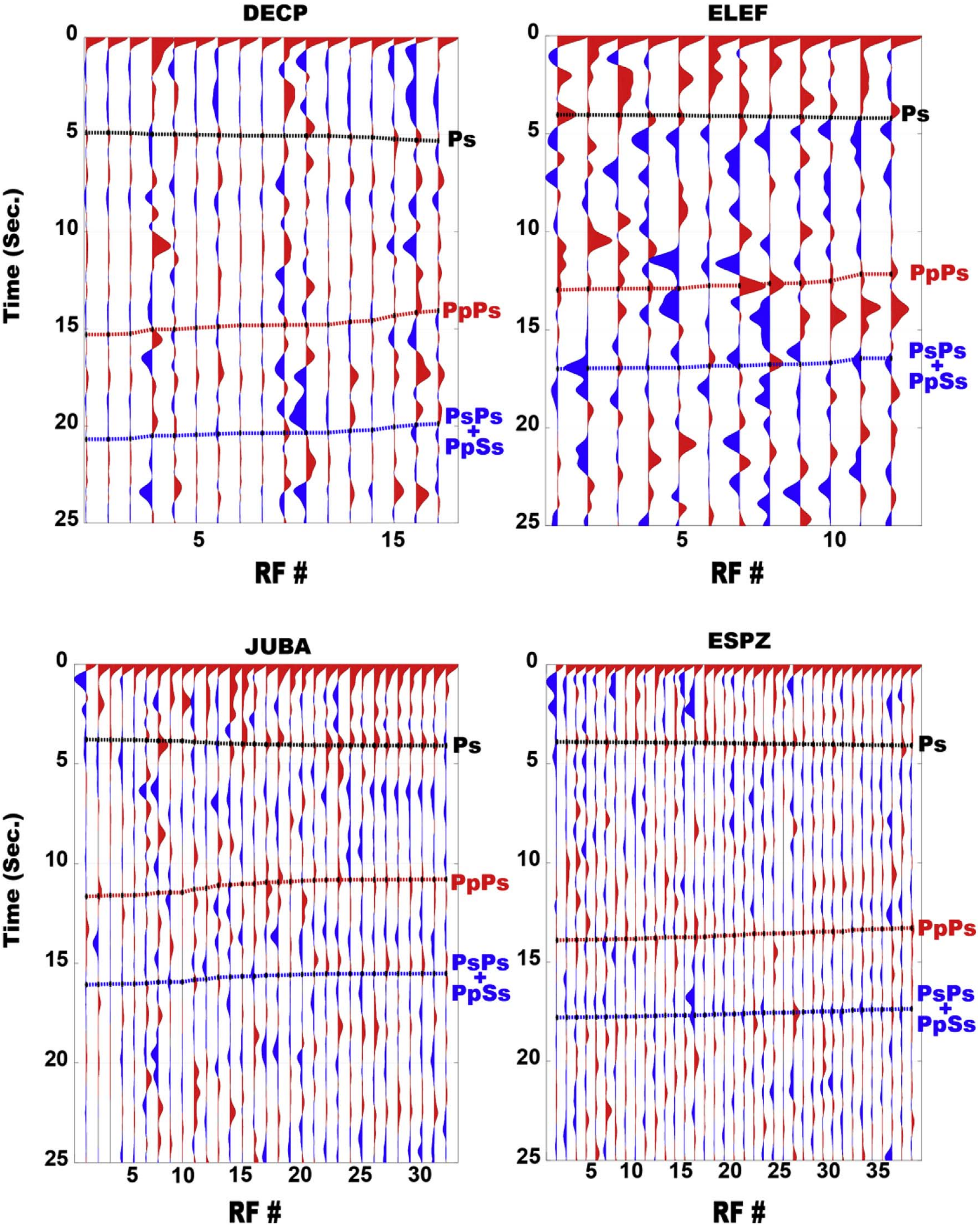

Fig. 3. Plots of receiver function sets for DECP, ELEF, JUBA and ESPZ calculated with 2.5 Hz Gaussian corner frequencies. Note the coherence in the arrival times and waveforms of the converted phases between 0 and 5 s for individual stations. Theoretical arrival times of Moho converted phase (Ps) and Moho associated multiples (PpPs and PsPs + PpSS) are also marked with dashed lines and are labeled.

assess the robustness of the results, we also calculated RFs with a Gaussian corner frequency of 1 Hz (Fig. 4). Compared to 2.5 Hz RFs, the 1 Hz RFs are less prone to higher frequency noise and arrivals that result from scattering. However, due to the larger width of the convolved pulse, they also yield coarser RFs with less well-constrained depth (or timing) estimates of Moho conversions or other crustal conversions (i.e. Calkins et al., 2006). Therefore, we mainly describe and interpret our results using RFs calculated using Gaussian corner frequencies of 2.5 Hz as these provide similar but better resolved converted phases.

Stacking of receiver functions is an effective way of eliminating noise and spurious phases that could be mistaken for a crustal or upper mantle discontinuity. An effective method of stacking is the H-κ-stacking. This procedure is considered a standard method for the determination of crustal thickness and Vp/Vs utilizing receiver functions (Zhu and Kanamori, 2000). H-κ-stacking combines information from multiple receiver functions computed at a given station and makes use of maximization of signal-to-noise ratio through systematic stacking of RFs. At the same time, H-κ stacking addresses the trade-off problems between crustal thickness and Vp/Vs if we were to use information from a single converted phase (Ps) rather than the combination of

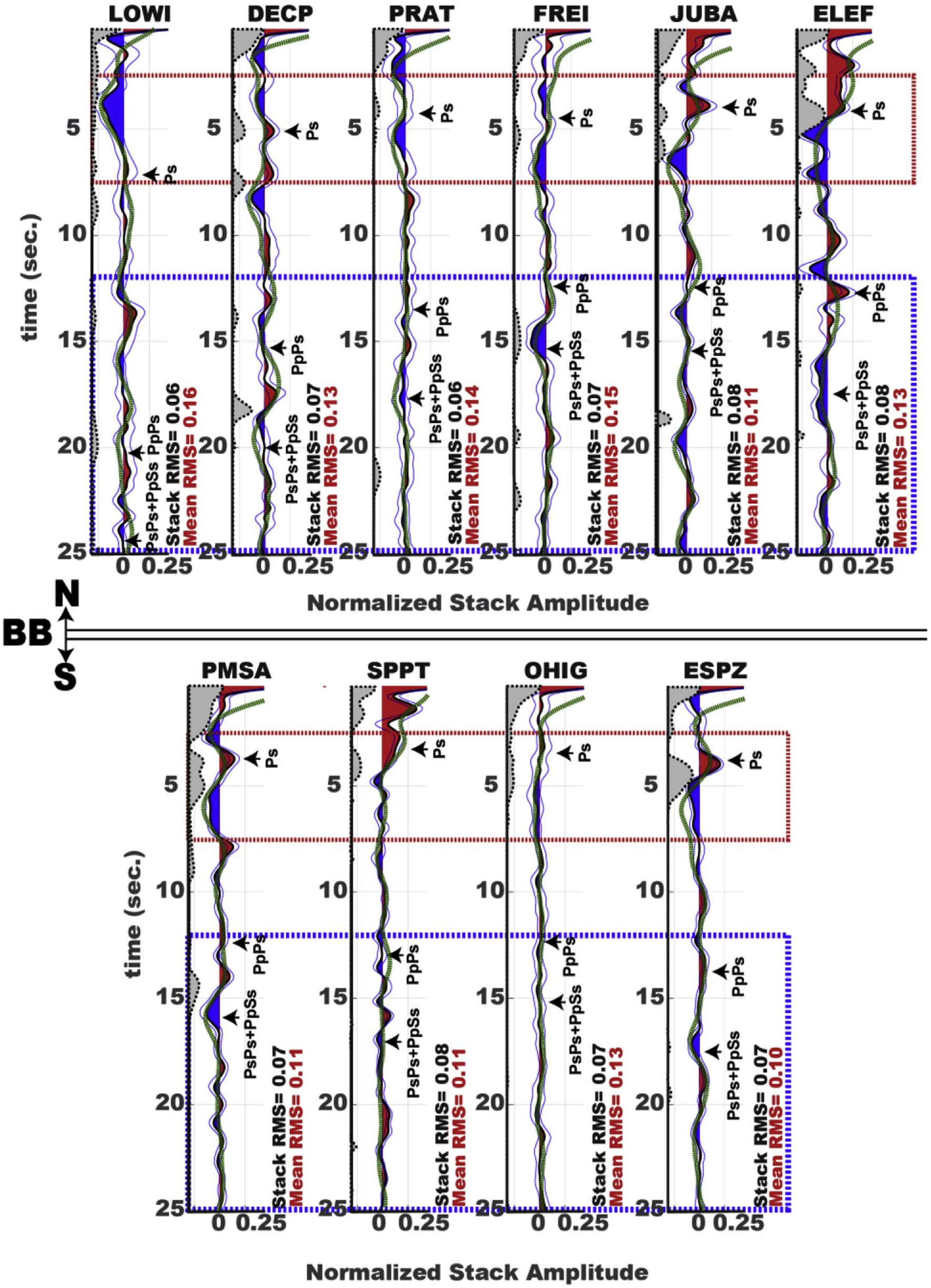

Fig. 4. Linear stacks of receiver functions with 2.5 Hz Gaussian corner frequency (patterns defining the bounds of blue and red patches). In addition, the stacks of RFs with 1 Hz Gaussian corner frequency are also shown for comparison as thick, dark green dashed lines. The top panel shows the stacks of RFs north of the BB and the bottom panel shows stacks belonging to the AP stations. The light blue lines that follow the RF marks the 0.5 standard deviations for the given time sample for the stacked ensemble. Also shown are the mean RMS values of the stacked RFs as well as RMS of the linear stack. On the left side of each RF stack a plot of cumulative phase coherency exceeding the median phase coherency of the stack are shown (gray bumps with dashed black outlines). This shows the robustness of the signals at the associated time window. Also shown are mean theoretical arrival times of Moho converted phases (Ps) and associated multiples (arrowheads labeled Ps, PpPs and PsPs + PpSs).

information from primary converted phases (Ps) and their reverberations in the crust (PpPs and PsPs). This approach comprises a parameter space search for Vp/Vs and crustal thickness that best explains the arrival time of direct Ps phase as well as the reverberations. Readers are referred to Zhu and Kanamori (2000) for further explanation of the H-κ stacking methodology. The accurate H-κ stacking of the RFs also requires incorporation of mean crustal Vp for individual stations. The average Vp values used for calculation of H-κ stacks are shown in Fig. 2c, next to each station. These mean Vp values agree well with the crustal Vp model of Maurice et al. (2003), who noted the significant heterogeneity in Vp structure of the region and derived individual models for each tectonic domain constituting the SSI and AP.

These receiver functions, together with the H-κ-stacks give us the ability to determine the geology beneath the stations deployed near BB and AP. The determination of the Vp/Vs of the lithosphere yields very valuable information about the rheology beneath each station. Furthermore, the accurate determination of the crustal thicknesses in the vicinity of each station allows us to obtain a better understanding of structural and dynamic controls on plates near active plate boundary zones.

3. Results

3.1. Receiver functions

In this section, we describe the receiver functions with 2.5 Hz corner frequencies (Figs. 3 and 4). We mainly describe the major attributes of the receiver functions using linear stacks of these for each of the 10 stations. We further investigate the complexity and noise content of RFs using root-mean-square (RMS) amplitudes of individual RFs compared to the RMS of linear stacks of RFs. We also identify robust arrivals that are common to all RFs making up the stack using the phase coherency of RFs.

The visual quality assessment of the receiver function datasets for each station yielded significant variations in the total number of receiver functions for these stations. This is primarily due to the variations in the noise levels and operation durations of these stations (Fig. 3). In general, the final receiver function datasets yielded a robust set of arrivals within first 5–10 s of the direct P arrival (Fig. 3). These arrivals mainly have positive amplitudes, especially closer to ~5 s, clearly indicating an upward reduction in seismic velocities and existence of significant discontinuities marking these zones of seismic velocity change (i.e. JUBA and ELEF in Fig. 3). One can also observe robust negative arrivals within first 5 s of the direct P arrival that mark top of the low-velocity zones and existence of higher seismic velocities closer to the surface (i.e. DECP and ESPZ in Fig. 3). Other coherent signals are present for the time range of 5–25 s (Fig. 3). These arrivals could be indicators of deeper structure or reverberations within the crust. H-κ-stacking and depth migration of receiver functions helps us to differentiate between structures and possible reverberations.

The linear stacks of receiver functions are useful in identifying arrival times of converted phases from major crustal discontinuities such as the Moho. One major advantage of stacking is the elimination of noise as well as the elimination of crustal reverberations as these reverberations tend to have significant amplitude and arrival time variations and likely cancel each other out in the process of stacking (Helffrich and Thompson, 2010). However, factors such as the dip of the converting interface and anisotropy can affect the arrival times and amplitudes of the arrivals, yielding incoherent stacking and hence diminishing of the arrival. In these cases, there may be a need for an additional constraint on the amplitude-unbiased coherency of the arrivals in a given time window. In such cases, the instantaneous phase of the arrival helps us better identify those phases that exist coherently in a time window but with significant variations in amplitude (Schimmel and Paulssen, 1997). Hence, calculation of instantaneous phase terms through Hilbert Transform of the analytic signal (the receiver function) allows us to estimate an additional measure of coherency and robustness for the entire receiver function (Schimmel and Paulssen, 1997; Helffrich and Thompson, 2010). In Fig. 4, we show both the linear stacks of receiver functions (red and blue arrivals) and cumulative instantaneous phase terms that exceed the median of the receiver function ensemble for given station (gray bumps with dashed outlines). Similar to individual receiver functions in Fig. 3 these also show significant positive amplitude arrivals at about 5 ± 2.5 s of the receiver function (red dashed box in Fig. 4). It is important to note that the phase coherency terms also dominate this portion of the receiver functions indicating the robustness of the arrivals in this time window (Fig. 4). We note that there exist coherent positive arrivals in the time window between 6 and 12 s, indicating the possible presence of deeper structures in the uppermost mantle or reverberations associated with intracrustal interfaces. Furthermore, coherent positive and negative arrivals exist later in the RFs at times greater than 12 s (blue dashed box in Fig. 4). This indicates that Moho associated multiples (PpPs, PsPs and PpSs) possibly exist in in this time window (labeled arrows in Fig. 4). It is also worth noting that the variations in complexity and timing of the arrivals are more pronounced for the stations along the island arc (top panel of Fig. 4) compared to the stacks of receiver functions of the AP (bottom panel of Fig. 4). However, in general, there exists a significant consistency between RFs calculated using Gaussian corner frequencies of 2.5 and 1 Hz, indicating the consistency and robustness of the results.

In general, the mean RMS values of receiver function gathers and stack means RMS values are similar across the stations (Fig. 4). However, some stations show distinctly lower stack RMS values compared to the mean RMS of the constituting Receiver functions. Good examples for these are, LOWI, FREI, and PRAT. These stations are located either on fairly isolated smaller islands or very close to the shoreline and are prone to noise compared to the remaining stations. It is possible that the stacks have relatively lower amount of noise due to the random nature of the noise. In general, the mean RMS of the individual stations is larger than the RMS of the stacks. This generally indicates the linear stacking effectively removes the spurious signals yielding more robust stacks. Hence, these stacks are more suitable for interpreting structures and crustal thickness in the study area. Furthermore, the island arc stations (north of BB) display higher mean RMS values (Fig. 4). This is possibly due to structural complexity beneath these stations as these are located very close to the former plate margin. Hence, the relatively higher RMS values point to the complexity of the crustal structure in the northern flank of the incipient rift. Most of the high mean RMS (0.13–0.16) stations located along the SSI display deeper signals at between 10 and 20 s consistently. This could be a mantle feature giving the complexity to the observed receiver functions at these stations.

3.2. H- κ stacks

Here, we present the results of H-κ-stacking approach at all stations in our study. We use these stacks for the determination of the crustal thickness and Vp/Vs of the crust beneath each station (Fig. 5). These stacks indicate the variability of the crustal thickness across the region. Particularly a significant variation exists in N-S direction across the center of the BB. Furthermore, significant variations are also visible across Eastern and western boundaries of SSB.

Most H- κ stacks are complicated with various crustal reverberations that have not been taken into consideration in the current approach of stacking. This significantly complicates the stacks and makes it difficult to determine an accurate crustal thickness and average Vp/Vs. In such cases, it is better to constrain the H- κ stacks in a narrower window of interest around the viable values of crustal thickness and Vp/Vs (Fig. 5). Furthermore, the character of the major reverberations (PpPs, PsPs and PsSs) that were taken into account in H- κ stacks significantly influences the nature of the H-κ stacks. If these reverberations are not strong enough due to scattering or structural complexity, then the Ps arrival can overprint these, giving more emphasized trade-off in H-K plots. A good

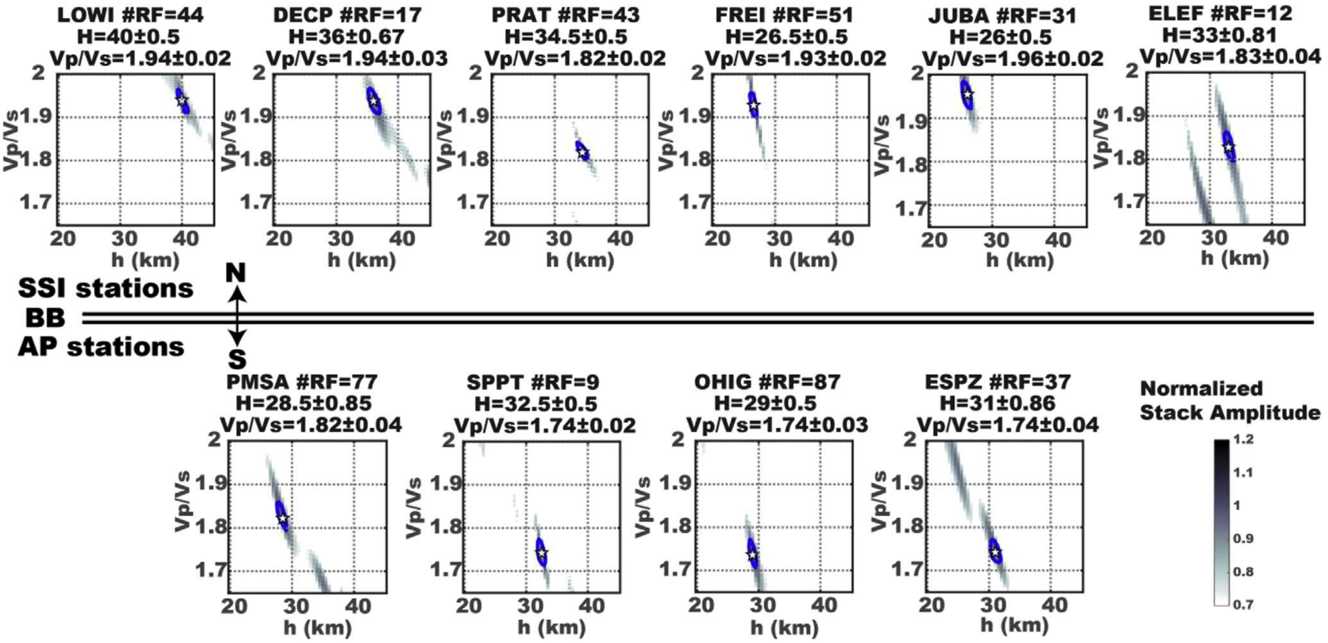

Fig. 5. H-κ stacks identifying crustal thickness (H) and bulk Vp/Vs (κ) beneath each station shown as open stars. The top panel represents the stations along the island arc (North of BB) and the bottom panel shows results for stations located on the AP. Results indicate a general consistency within subsets belonging to northern and southern part of the study area (North and south of BB). The blue contours indicate 95% confidence interval for the maximum stack amplitude.

example will be the comparison of H- κ plots of JUBA and FREI, where the noisier FREI yields a more significant trade-off between Vp/Vs and crustal thickness while higher SNR stack of JUBA yield a fairly better determined Vp/Vs and crustal thickness. In general, the H- κ stacking yield reliable estimates of Vp/Vs and crustal thickness for the region. These show significant variations and a trade-off in the north of the BB while more consistent results in the south along the AP (Fig. 5).

4. Discussion

4.1. *Limitations and resolution*

An appraisal of linearly stacked RFs illustrates the need to consider noise-reduction practices even for high-quality, densely sampled stations like PMSA. While RFs of most stations reveal coherent features in the crust and upper mantle, they also contain less-coherent secondary arrivals, which are important in H-κ stacks. The source of signal-generated noise here likely results from the complicated geologic and tectonic setting. Particularly, Cenozoic-age volcanic cover, dense extensional structures and related sedimentation along the border with the basin, characterizes the island arc portion of the study area. We suspect, these significantly mask the primary features of the RFs here. Never the less, we observe consistent arrivals at the theoretical arrival times of Moho conversions (Ps) and multiples (PpPs and PsPs + PpSs) calculated using crustal thickness and Vp/Vs ratios obtained using the H-κ stacks. We observe this clear correlation and consistency between individual RFs (dashed lines in Fig. 3) as well as between stacks of RFs using 1 and 2.5 Hz Gaussian corner frequencies (Fig. 4).

Unlike conventional travel time tomography results the signal presented in RFs indicate the depth of the interfaces that the converted phase arrives from. The lateral resolution in RFs is controlled by the location of the impinging ray, hence depends on the accuracy of the ray tracing procedure. Since these arrivals have significantly steep incidence angles, their piercing points can be determined with sufficient accuracy via simple minimum travel-time ray tracing methodologies using simple 1-D velocity models. On the other hand, the vertical resolution depends heavily on the character of Gaussian filter/pulse that is used during the iterative deconvolution stage. In terms of wavelength, which controls the vertical resolution recoverable in the receiver functions, a corner of 2.5 Hz corresponds to crustal wavelengths greater than roughly 2.7 km.

Never the less, from both the linear stacks (Fig. 4) and the H-κ stacks (Fig. 5) it is clear that there exist systematic variations in shallower (< 5 s) portions of the study area, which are more pronounced regardless of limitations in resolution and existence of spurious signals. This is clearly indicated by the higher cumulative coherency at these portions of the RFs. Hence, these variations point at the complexity of the structure along the northern flank of the rift, closer to the plate boundary. This complexity also agrees well with the segmentation of the BB and SSB inferred form shallow crustal structure of the region (Grad et al., 1992; Lawver et al., 1995, 1996; Vuan et al., 2001).

4.2. *Depth migrated receiver function stacks*

Convenient ways to look at computed receiver functions are the depth migrated stacks which provide a better sense of location compared to RFs in the time domain (Fig. 6). We calculated these stacks using the Vp/Vs and crustal thickness values determined via H-κ stacking. These stacks indicate once more that there exists significant variations in crustal and upper mantle structure in the region upon a comparison of the depth migrated RFs (Fig. 6). This is most clear when the receiver functions belonging to the northern and southern flank of the BB are compared. We observe that the stacks of RFs (both depth migrated, linear and H- κ) show similar results for the AP but fairly significant variations for the SSI (Fig. 6). We argue that this primarily points to the asymmetric nature of the basin that is also evident in the bathymetry (Fig. 1). It is clear that while the AP is less affected by the incipient rifting of BB along the trend of the peninsula the South Shetland Pedestal is significantly deformed and segmented closer to the subduction margin. It is also very surprising that it is not the southern but the northern flank of the rift (BB) that marks the thickest crust of the study area. This possibly indicates the intensity and the complexity of deformation along the South Shetland Pedestal and the interior of the SSB. In the following sections, we discuss the products of this deformation in detail.

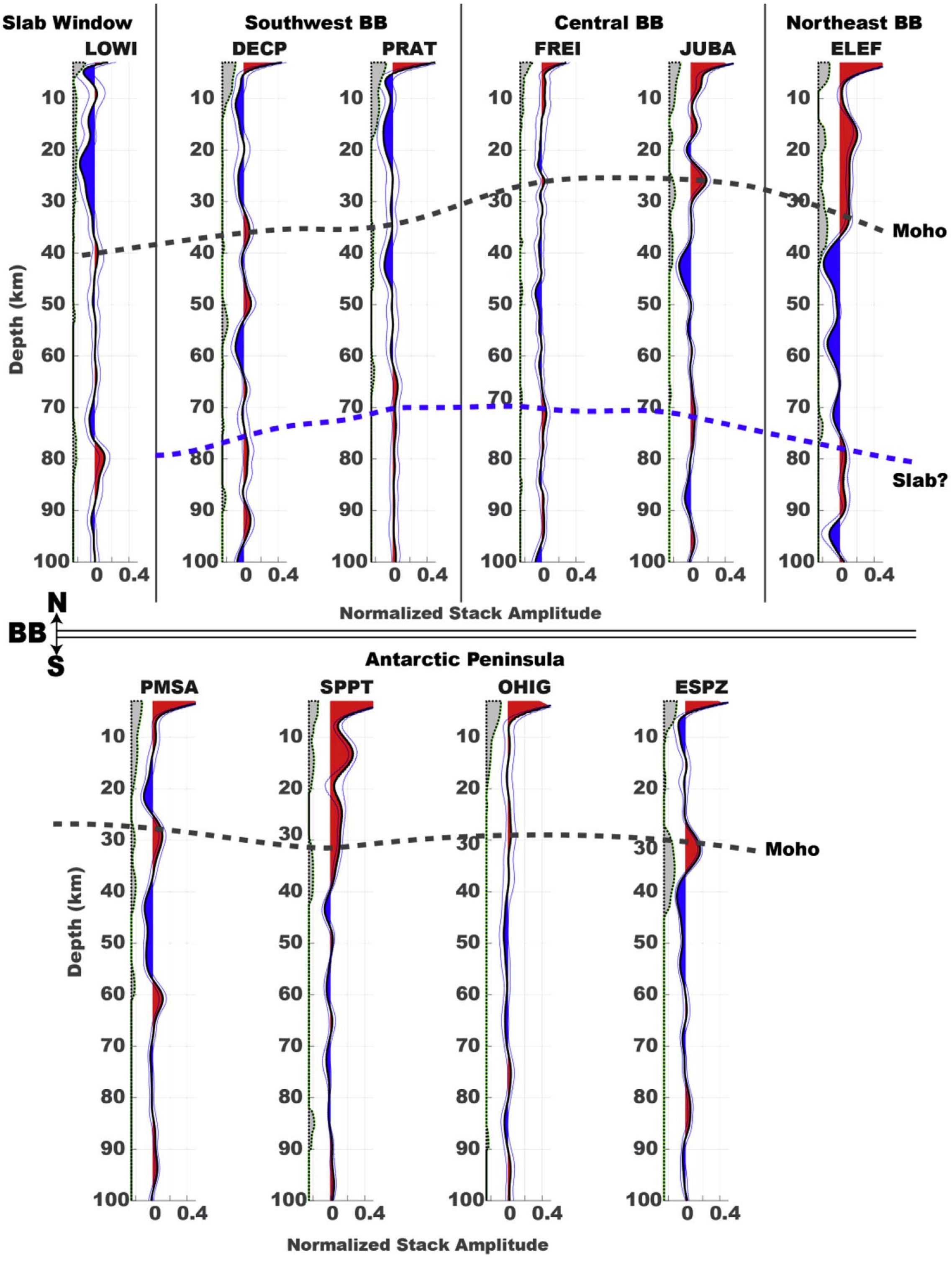

Fig. 6. Depth migrated stacks of receiver functions for each station of the study area. The top panel represents the RFs for stations along the island arc (North of BB) and the bottom panel shows RFs belonging to the AP. The bold black dashed line shows the depth to Moho at each RF. The depth to slab inferred from a coherent deep converted phase is also marked by dashed bold blue line. On the left side of each RF stack a plot of cumulative phase coherency exceeding the median phase coherency of the stack are shown.

4.3. Thickness of the South Shetland Block

Both H-κ results and migrated RFs show systematical variations in the region that agrees well with the tectonic setting of the area. Results suggest the crust is thinning from 30 km to 26 km from the AP towards the South Shetland trench near the central BB (Figs. 6 and 7). Even though we do not have any stations directly in the BB it has been shown in various studies that the center of the basin marking the recent volcanic zone is significantly thin in accord with extension related thinning of the incipient rift (Vuan et al., 2001; Grad et al., 1992; Christeson et al., 2003).

Furthermore, our results indicate that the crust thickens towards the southwestern and northeastern boundary of the SSB and in the southwestern BB. In an earlier study by Bird at al. (2000) these regions were

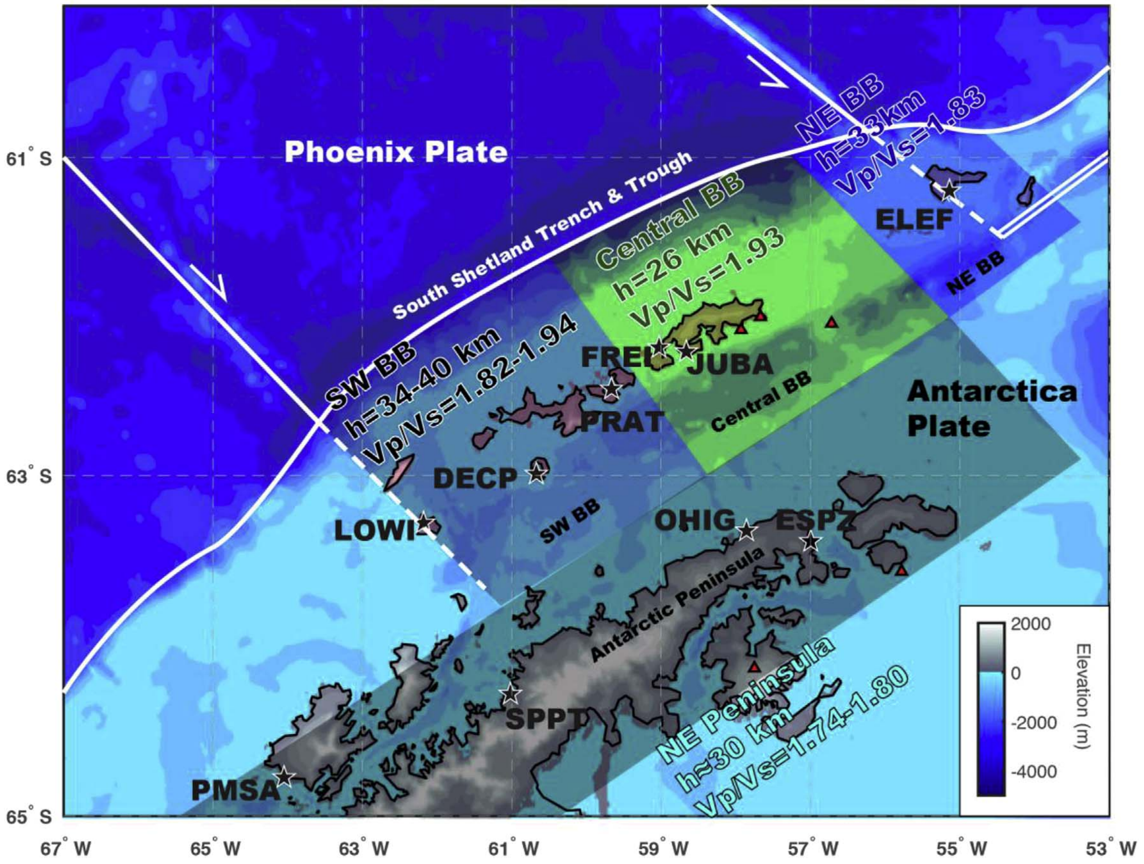

Fig. 7. Map summarizing crustal thickness variations across the study area along with the variations in Vp/Vs. The results clearly show the segmentation of not only the BB but also on a larger scale the SSB. Note that the AP is relatively less complex in this framework indicating limited deformation upon initiation of the rifting and perhaps the opening of the slab window.

pointed out as possible boundaries of the SSB. The significant thickness variations in these zones compared to the central parts of the BB agrees well with this plate model. We would expect plate boundary zones to be associated with significant variations in crustal heterogeneity and thickness due to the interaction between plates. Hence, both the northeastern and the southwestern margins of the SSB could have attained thickened crust characteristics due to plate reconfiguration (Fig. 7).

In addition, the opening of slab window beneath the southwestern margin and the associated thermal weakening of the overriding crust may be a contributor in this significant variation in crustal thickness of the SSB. We acknowledge that the crust is uncharacteristically thick (~40 km) beneath the southwestern. In order for this region to attain isostatic compensation, there needs to be a pronounced surface topography reaching 1–2 km above sea level and/or the region requires dense crustal roots. Interestingly, this region constitutes Smith Island (SI in Fig. 1) with peaks reaching up to ~1.8 km. We argue that opening of the slab window may partly explain the underplating of hot asthenosphere and emplacement of denser roots through metasomatism and deformation along the southwestern bound of SSB. The probable emplacement of hot asthenosphere with lower P-wave speeds beneath the crust reduces the seismic impedance contrast between crust and mantle. This could be the reason for the smaller amplitude and hence, less distinguishable, Moho arrivals (Ps) observed at LOWI compared to nearby stations or stations located along the AP (e.g. ESPZ) (Figs. 4 and 6).

The observation of relatively thinner crust in the northeastern boundary of the SSB also agrees with the observations from wide-angle reflection surveys as well as surface wave studies (Vuan et al., 2001; Christeson et al., 2003). Hence, our results agree with many of the previous studies that rifting of the Antarctic Plate margin is progressed from NE towards SW. However, the variations of the crustal thickness along the Island Arc also indicates the opening of the slab window and the rollback of stalled slab plays an important role in controlling the evolution of the rift basin (BB). We would expect the thinner part of the basin to be located near the center of the SSB and central BB, near which the rollback of the stalled Phoenix slab is more prominent and yields relatively higher rates of extension as inferred from variations in trench-ward plate deformation rates across the SSB (Taylor et al., 2008) and the arcuate geometry of the SST (Fig. 1).

4.4. *Structure of the BB and SSB*

High Vp/Vs ratios (~1.82–1.96) beneath BB and SSI, agree well with the incipient crustal rift character of BB and the presence of partial melts (Vuan et al., 2005). This is especially clear along the South Shetland Pedestal. The presence of partial melts also agrees with the observations of the steep nature of the slab here inferred from tomography (Park et al., 2012). We would expect the slab to be between 60 and 100 km depth beneath this region. Our depth migrated RF stacks indicate the presence of clear arrivals at depths ~70–80 km beneath LOWI, DECP, PRAT, JUBA FREI and ELEF (Fig. 6). In general, Moho associated multiples follow the Ps phase and can be mistaken for deep structures. However, the calculated theoretical times of these multiples (PpPs, PsPs and PpSs) exceeds 12 s for the RFs computed in this study (see labeled arrows in Fig. 4). Hence, these multiples generally map to depths in excess of 100 km and do not overlap with arrivals observed between 70 and 80 km depth range. The timing and the migrated depth of the associated arrivals agree well with the imaged depth of the stalled Phoenix slab beneath the SSI (Park et al., 2012). Hence, we speculate that these clear arrivals mark the oceanic Moho of the Phoenix slab beneath the region. The clear coherence of the signal

(Fig. 6) and the robust amplitude indicates that the impedance of the converting boundary is significant and hence much stronger and coherent than the amplitudes of the possible crustal reverberations that may be arriving around the same time as these signals. Converted phases from deeper regions are not present beneath the stations of the AP indicating the slab must be significantly steep. We should also note that this region is also located very close to the trench (SST). It is hence, natural to expect a steep slab beneath the region, which calls for a wide mantle wedge, a wider zone of serpentinization, and hence a wider volume for partial melting to take place closer to the trench. Hence, this setup can explain not only the higher Vp/Vs values in the northern flank of the incipient rift that is quite different from the southern margin, but also the asymmetric nature of the BB with a broader southern margin (near AP) but a narrower deformation zone associated with the northern margin (near South Shetland Pedestal).

Further more, significant variations in crustal thickness and Vp/Vs ratio point to the heterogeneity of the crustal structure of the SSB while AP is relatively more homogeneous. A RF study by Vuan et al. (2001) also revealed the crustal thickness varies less along the AP. They calculated a crustal thickness of 37 km for ESPZ and 40 km for PMSA. This is significantly different from our findings of 32 km for ESPZ and 30 km for PMSA. However, Vuan et al. (2001) also noted that these results are preliminary and more accurate results require more RFs and a better back azimuthal coverage.

The strong segmentation of the crust in the study area has already been proposed for the region in various studies (Grad et al., 1992; Gracia et al., 1996; Christeson et al., 2003; Maurice et al., 2003). Our RFs show strong agreement between such segmentation of both BB and SSB into the southwest, central and northeast segments (Gracia et al., 1996) and the systematic variations in Vp/Vs and crustal thickness (Fig. 7). We also note that there exist significant variations in the amplitude of the Moho arrivals (Ps) across the study area. This indicates the variations in the seismic speeds and density of lithologies above and below crust-mantle interface hence, the heterogeneity in the upper mantle, and/or lower crustal compositions, thermal properties and partial melt content. Hence, this heterogeneity also agrees well with the scale and intensity of segmentation of BB and SSB. Based on these observations we infer that the deeper structure beneath the BB and SSB, characterized by the Phoenix slab and the slab windows in the southwest and possibly in the northeast, has a significant control on the segmentation of the crust in the region, controlling mainly the geometry and deformation of the SSB and BB. In contrary to SSB and BB, the observed crustal thicknesses, Vp/Vs and Moho conversion amplitudes do not show a systematic and significant variation across the AP, indicating upper mantle tectonic controls that partition the BB and SSB has a less recognizable effect on the AP (Fig. 7). This is in good agreement with the asymmetry of the BB with the major crustal deformation zones being closer to the SSI rather than the AP (Barker et al., 2003; Maurice et al., 2003) (Figs. 1 and 7).

5. Conclusions

Our receiver functions clearly indicate significant variations in crustal thickness at the boundaries of the SSB. We interpret these variations to be the clear indication of active deformation of the SSB by ongoing rifting along BB and subduction rollback along South Shetland Trench. This is in good agreement with the higher-levels of seismicity and tectonism along this portion of the Antarctic plate boundary. These observations are also supported by the strong variations in the Vp/Vs ratio of crust, indicating significant crustal heterogeneity.

The receiver functions in the BB and SSB reveal significant variations and complexity across the region. This indicates the significant complexity of the lithospheric and upper mantle structure in the region. This is mainly manifested by the strong segmentation of the SSB as shown by earlier wide-angle reflection and deep sounding surveys. Based on significant variations in crustal thickness and Vp/Vs revealed by our RFs, we interpret that the deeper configuration of the Phoenix slab and the slab windows that bounds it are responsible for the segmentation of the volcanic arc crust and control the structure of the SSB as well as distribution of the deformation along the BB.

Based on our results and observations from receiver function analysis we propose that opening of the slab window, present rifting along Bransfield Basin and stalling subduction of Phoenix slab control the evolution and present deformation of the SSB. A better understanding of the crustal and lithospheric structure and tectonics of this region relies heavily on the improved broadband seismic data coverage in the region through temporary and permanent seismic deployments.

Acknowledgements

This research was performed while the author CB Biryol held an NRC Research Associateship award at U.S. Army Research Laboratory/Army Research Office. The facilities of IRIS Data Services, and specifically the IRIS Data Management Center, were used for access to waveforms, related metadata, and/or derived products used in this study. IRIS Data Services are funded through the Seismological Facilities for the Advancement of Geoscience and EarthScope (SAGE) Proposal of the National Science Foundation under Cooperative Agreement EAR-1261681.

Appendix A. Supplementary data

Supplementary data related to this article can be found at http://dx.doi.org/10.1016/j.polar.2018.02.003.

References

Alfaro, P., Lopez-Martinez, J., Maestro, A., Galindo-Zaldivar, J., Duran-Valsero, J., Cuchi, J., 2010. Recent tectonic and morphostructural evolution of byers peninsula (Antarctica): insight into the development of the south Shetland islands and Bransfield basin. J. Iber. Geol. 36 (1), 21–37.

Ashcroft, W.A., 1972. Crustal structure of the south Shetland islands and Bransfield Strait. Brit. Antarct. Surv. 66.

Baranov, A., Morelli, A., 2013. The Moho depth map of the Antarctica region. Tectonophysics 609, 299–313.

Barker, P.F., Dalziel, I.W.D., 1983. Progress in geodynamics in the scotia arc region. In: In: Cabré, R. (Ed.), Geodynamics of the Eastern Pacific Region, Caribbean and Scotia Arcs, vol. 9. Geodynamics Series American Geophysical Union Series, pp. 137–170.

Barker, D.H., Austin, J.A., 1998. Rift propagation, detachment faulting, and associated magmatism in Bransfield strait, Antarctic Peninsula. J. Geophys. Res.: Solid Earth 103 (B10), 24017–24043.

Barker, D.H.N.G.L., Christenson, Austin, J.A., 2003. Backarc basin evolution and cordilleran orogenesis: insights from new ocean-bottom seismograph refraction profiling in Bransfield Strait, Antarctica. Geology 31, 107–110.

Birkenmajer, K., Delitala, M.C., Narebski, W., Nicoletti, M., Petrucciani, C., 1986. Geochronology of tertiary island-arc volcanics and glaciogenic deposits, king george island, South Shetland islands (west Antarctica). Pol. Acad. Sci. Earth Sci. 34, 257–273.

Breitsprecher, K., Thorkelson, D.J., 2009. Neogene kinematic history of Nazca– antarctic–phoenix slab windows beneath Patagonia and the Antarctic Peninsula. Tectonophysics 464 (1), 10–20.

Calkins, J.A., Zandt, G., Gilbert, H.J., Beck, S.L., 2006. Crustal images from San Juan, Argentina, obtained using high frequency local event receiver functions. Geophys. Res. Lett. 33 (7).

Christeson, G.L., Barker, D.H., Austin, J.A., Dalziel, I.W., 2003. Deep crustal structure of Bransfield Strait: initiation of a back arc basin by rift reactivation and propagation. J. Geophys. Res-Sol. EA 108 (B10).

Civile, D., Lodolo, E., Vuan, A., Loreto, M., 2012. Tectonics of the Scotia–Antarctica plate boundary constrained from seismic and seismological data. Tectonophysics 550, 17–34.

Dalziel, I.W.D., 1984. Tectonic evolution of a forearc terrane, southern scotia ridge. Geol. Soc. Am., Spec. Pap. 200, 32.

Dietrich, R., Dach, R., Engelhardt, G., Ihde, J., Korth, W., Kutterer, H.-J., Lindner, K., Mayer, M., Menge, F., Miller, H., et al., 2001. ITRF coordinates and plate velocities from repeated GPS campaigns in Antarctica–an analysis based on different individual solutions. J. Geodesy 74 (11–12), 756–766.

Galindo-Zaldivar, J., Gamboa, L., Maldonado, A., Nakao, S., Bochu, Y., 2004. Tectonic development of the bransfield basin and its prolongation to the south scotia ridge, northern antarctic peninsula. Mar. Geol. 206 (1), 267–282.

Gonzalez-Ferran, O., 1985. Volcanic and tectonic evolution of the northern Antarctic Peninsula—late Cenozoic to recent. Tectonophysics 114 (1), 389–409.

Gracia, E., Canals, M., Farran, M.L., Prieto, M.J., Sorribas, J., Team, G., 1996.

Morphostructure and evolution of the central and eastern bransfield basins (NW Antarctic Peninsula). Mar. Geophys. Res. 18 (2–4), 429–448.

Grad, M., Guterch, A., Sroda, P., 1992. Upper crustal structure of deception island area, Bransfield Strait, west Antarctica. Antarct. Sci. 4 (04), 469–476.

Guillaume, B., Moroni, M., Funiciello, F., Martinod, J., Faccenna, C., 2010. Mantle flow and dynamic topography associated with slab window opening: insights from laboratory models. Tectonophysics 496 (1), 83–98.

Hansen, S.E., Graw, J.H., Kenyon, L.M., Nyblade, A.A., Wiens, D.A., Aster, R.C., Huerta, A.D., Anandakrishnan, S., Wilson, T., 2014. Imaging the Antarctic mantle using adaptively parameterized p-wave tomography: evidence for heterogeneous structure beneath west Antarctica. Earth. Planet. Sc. Lett. 408, 66–78.

Helffrich, G., Thompson, D., 2010. A stacking approach to estimate Vp/Vs from receiver functions. Geophys. J. Int. 182 (2), 899–902.

Hole, M., Larter, R., 1993. Trench-proximal volcanism following ridge crest-trench collision along the Antarctic Peninsula. Tectonics 12 (4), 897–910.

Keller, R.A., Fisk, M.R., White, W.M., Birkenmajer, K., 1991. Isotopic and trace element constraints on mixing and melting models of marginal basin volcanism, Bransfield Strait, Antarctica. Earth Planet Sci. Lett. 111, 287–303.

Larter, R.D., Barker, P.F., 1991. Effects of ridge crest-trench interaction on Antarctic-Phoenix spreading: forces on a young subducting plate. J. Geophys. Res. 96 19,583–19,607.

Lawver, L.A., Keller, R.A., Fisk, M.R., Strelin, J.A., 1995. Bransfield strait, Antarctic Peninsula Active Extension Behind a Dead Arc. Backarc Basins. pp. 315–342.

Lawver, L.A., Sloan, B.J., Barker, D.H., Ghidella, M., Von Herzen, R.P., Keller, R.A., Klinkhammer, G.P., Chin, C.S., 1996. Distributed, active extension in Bransfield basin, Antarctic Peninsula: evidence from multibeam bathymetry. GSA Today 6 (11), 1–6.

Ligorria, J.P., Ammon, C., 1999. Iterative deconvolution and receiver-function estimation. B. Seismol. Soc. Am. 89 (5), 1395–1400.

Majdański, M., Środa, P., Malinowski, M., Czuba, W., Grad, M., Guterch, A., Hegedús, E., 2008. 3D seismic model of the uppermost crust of the admiralty bay area, king george island, west Antarctica. Pol. Polar Res. 29 (4), 303–318.

Machado, A., Chemale, F., Conceição, R.V., Kawaskita, K., Morata, D., Oteíza, O., Van Schmus, W.R., 2005. Modeling of subduction components in the genesis of the meso-cenozoic igneous rocks from the south Shetland arc, Antarctica. Lithos 82 (3), 435–453.

Maurice, R.S.D., Wiens, D.A., Shore, P.J., Vera, E., Dorman, L.M., 2003. Seismicity and tectonics of the south Shetland islands and Bransfield Strait from a regional broadband seismograph deployment. J. Geophys. Res-Sol. EA 108 (B10).

McCrory, P.A., Wilson, D.S., Stanley, R.G., 2009. Continuing evolution of the Pacific-Juan de Fuca-North America slab window system - a trench-ridge-transform example from the Pacific Rim. Tectonophysics 464, 30–42.

Park, Y., Kim, K.-H., Lee, J., Yoo, H.J., et al., 2012. P-wave velocity structure beneath the northern Antarctic Peninsula: evidence of a steeply subducting slab and a deep-rooted low- velocity anomaly beneath the central Bransfield basin. Geophys. J. Int. 191 (3), 932–938.

Schimmel, M., Paulssen, H., 1997. Noise reduction and detection of weak, coherent signals through phase-weighted stacks. Geophys. J. Int. 130 (2), 497–505.

Sell, I., Poupeau, G., Gonzalez-Casado, J., Lopez-Martinez, J., 2004. A fission track thermochronological study of king george and livingston islands, South Shetland islands (west antarctica). Antarct. Sci. 16 (02), 191–197.

Smellie, J.L., Pankhurst, R., Thomson, M., Davies, R., 1984. The geology of the south Shetland islands: VI. Stratigraphy, geochemistry and evolution. Brit. Antarct. Surv. 87 v. 87.

Taylor, F.W., Bevis, M.G., Dalziel, I.W., Smalley, R., Frohlich, C., Kendrick, E., Gudipati, K., 2008. Kinematics and segmentation of the south Shetland Islands-Bransfield Basin system, northern antarctic peninsula. Geochem. Geophy. Geosy. 9 (4).

Thorkelson, D.J., 1996. Subduction of diverging plates and the principles of slab window formation. Tectonophysics 255, 47–63.

van Wijk, J.W., Govers, R., Furlong, K.P., 2001. Three-dimensional thermal modeling of the California upper mantle: a slab window vs. stalled slab. Earth. Planet. Sc. Lett. 186, 175–186.

Vuan, A., Brancolini, G., Panza, G., Russi, M., Wu, F., 2001. Joint inversion of receiver function of teleseismic body waves and local group velocity dispersion curves beneath ESPZ and PMSA stations (Antarctic Peninsula). Terra Ant 8, 49–54.

Vuan, A., Maurice, S.D.R., Wiens, D.A., Panza, G.F., 2005. Crustal and upper mantle S-wave velocity structure beneath the Bransfield Strait (West Antarctica) from regional surface wave tomography. Tectonophysics 397, 241–259.

Zhu, L., Kanamori, H., 2000. Moho depth variation in southern California from teleseismic receiver functions. J. Geophys. Res-Sol. EA 105 (B2), 2969–2980.